Biomaterials Science

ROYAL SOCIETY OF CHEMISTRY

PAPER

View Article Online
View Journal | View Issue

Cite this: *Biomater. Sci.*, 2025, **13**, 6676

Re-osseointegration of titanium after experimental implant loosening

Martina Jolic, [a] Paula Milena Giraldo-Osorno, [a] Lena Emanuelsson,[a] Birgitta Norlindh,[a] Peter Thomsen, [a,b] Furqan A. Shah [a] and Anders Palmquist *[a]

This study addresses the critical clinical challenge of implant failures due to mechanical overload by developing a novel rat model to investigate re-osseointegration. Metal implants, essential in dental, maxillofacial, and orthopaedic treatments, rely on osseointegration for stability. However, the fate of mechanically overloaded implants remains poorly understood. We introduced intentional traumatic loosening of submicron-modified titanium implants (treated with NaOH) through snap rotational overload in rat tibiae. After four weeks of initial healing, implants were disrupted and then allowed to re-heal for another four weeks. Evaluations using removal torque, histology, histochemistry, and Raman spectroscopy demonstrated successful re-healing with regained mechanical stability, bone–implant contact, and bone volume. Dynamic histology revealed bone tissue remodelling near the implant interface, indicating fractures due to mechanical disruption. These findings confirm that osseointegrated implants can re-heal under normal conditions. The validated rat model offers a controlled platform for future studies on re-osseointegration following traumatic mechanical overload. The potential applications of this experimental model may extend to investigating compromised healing conditions, early/direct loading conditions, and the cellular and molecular mechanisms involved in peri-implant bone repair.

Received 2nd April 2025,
Accepted 8th October 2025

DOI: 10.1039/d5bm00502g

rsc.li/biomaterials-science

Introduction

In recent decades, metal implants have become a key treatment modality for restoring skeletal function and integrity in dental, maxillofacial, and orthopaedic applications. The long-term anchorage of metal implants is attributed to osseointegration, the mechanism by which bone forms a direct, functional connection with the implant without intervening soft tissue.[1,2] However, implant failures still occur and can result in a challenging clinical situation, often requiring revision surgery and increasing the risk of further health complications.

Known risk factors for implant failure include insufficient bone volume, poor bone quality, and mechanical overload.[3] Both bone quality and bone volume are critical determinants of long-term success of osseointegration, and have been investigated in the context of ageing,[4–6] systemic disease, and/or drug administration.[7–9] While mechanical loading of an implant can have either positive or negative consequences on the stability of osseointegrated implants and the peri-implant bone, the effects are highly dependent on the loading frequency, magnitude, and duration of the applied forces.[10–15] Although the effects of mechanical loads on implant osseointegration are continuously explored, the consequences of traumatic mechanical failure and the possibility of re-establishing osseointegration remain poorly understood.

Mechanical overload is often a primary trigger for mechanical failure, caused by events such as occlusal trauma[16–18] or sudden compressive forces in high-demand events like stumbling.[19] With growing reliance on use of metal implants for fracture fixation,[20] joint replacement,[21] and dental reconstructions,[22] a better understanding of re-osseointegration is of critical importance, particularly in an ageing society where trauma-induced failures are more likely. Research to date has not provided a comprehensive understanding of the underlying biological events following traumatic mechanical failure (*i.e.*, mechanical instability).[23] Clinical case reports suggest re-osseointegration is possible following mechanically caused failure in otherwise healthy dental patients,[24,25] and in a transtibial amputee with a bone anchored prosthesis.[26] Re-osseointegration of metal implants following a traumatic disruption of the bone–implant interface has only been demonstrated in a few reports in rabbits[27–29] and dogs.[30] All of these studies showed that re-healing allowed same or higher mechanical anchorage of disrupted implants, while presenting insufficient

[a]*Department of Biomaterials, Institute of Clinical Sciences, Sahlgrenska Academy, University of Gothenburg, Sweden. E-mail: anders.palmquist@biomaterials.gu.se*
[b]*Department of Biomedical Dental Sciences, College of Dentistry, Imam Abdulrahman Bin Faisal University, Saudi Arabia*

histological or mechanistic evidence. However, the impact of traumatic mechanical overload on metal implants remains understudied despite its clinical relevance.

The rat has been previously described as a suitable animal model for the evaluation of interface biomechanics,[31] offering advantages over larger species in cost, handling, and a short bone remodelling cycle, while still allowing reliable biomechanical and histological evaluation of osseointegration. Surface modification is a well-established approach to improve osseointegration of titanium implants. Micro- to nanoscale topographies promote bone growth kinetics and biomechanical anchorage,[32–34] and alkali treatment, in particular, produces a uniform, porous submicron titanate layer that has demonstrated a robust biomechanical fixation *in vivo*.[35–41] Owing to its simplicity and reproducibility, this method provides a reliable surface for evaluating bone–implant interactions. To date, no small-animal model has been established to study re-osseointegration following mechanical overload. Herein, we establish a rat model to investigate the effects of mechanical overload on implant stability using alkali-modified titanium implants, and determine the impact of traumatic implant failure on peri-implant bone microstructure and composition, healing, remodelling, and cellular response in re-osseointegration.

Materials and methods

Surface modification

The effect of alkali and heat treatment on the surface of commercially pure Ti (cp-Ti) was investigated using machined cp-Ti discs (grade IV, ∅ 9 mm, h = 1 mm). Individual discs were successively cleaned with Extran (Merck, Germany) and deionised water using ultra-sonication. Surface modification was performed by placing the discs in a 5M NaOH solution (Merck, Germany) at 60 °C for 24 hours. Following the alkali-treatment, the discs were thoroughly washed in deionised water. Half of the discs were dried at 200 °C for an additional 24 hours (heat dried, NaOH-HD) and the remaining half were dried at room temperature in a laminar airflow cabinet to protect the samples from particulate contamination (air dried, NaOH-AD). Heat exposure served as a dry sterilisation process. Characterisation of modified surfaces was performed on air dried and heat dried discs.

Screw-shaped cp-Ti (grade IV) implants (∅ 2 mm, 2 mm in length) with a cube head (1.4 × 1.4 × 1 mm) were successively cleaned and surface modified, as described above. Finally, all implants were heat dried at 200 °C for additional 24 hours in air. Implant cleaning and surface treatment were performed while maintaining clean conditions. To verify the absence of pyrogenic substances, the endotoxin test was performed on cleaned and heat dried implants (n = 3) showing an endotoxin level below the detection level, *i.e.*, <0.125 EU per device (Microbial Analytics Sweden AB, Sweden).

Surface characterisation

Alkali-modified cp-Ti discs and screws were imaged using scanning electron microscopy (SEM; Ultra 55 FEG SEM, Leo Electron Microscopy Ltd, UK) operated at a 5 kV accelerating voltage, and a 5 mm working distance. The thickness of the alkali-modified surface on NaOH-AD and NaOH-HD discs was determined using focused ion beam scanning electron microscopy (FIB-SEM; FEI Versa3D LoVac DualBeam, FEI Company, USA). Using Au sputter-coated samples (10 nm), the area of interest was protected by Pt deposition, followed by milling a rough trench (ion beam current 500–1.7 pA), and finally polishing the cross section at low beam current (50–300 pA). The Au coating enabled distinguishing between the Pt layer and the sample surface, allowing measurement of the thickness of alkali-modified surface using ImageJ (imagej.nih.gov/ij). The surface chemistry of NaOH-AD and NaOH-HD discs was evaluated using micro-Raman spectroscopy and energy dispersive X-ray spectroscopy (EDX). Using a confocal Raman microscope (Renishaw inVia Qontor, Renishaw plc, UK) equipped with a 785 nm laser and Live-Track focus-tracking technology, 100 μm^2 areas were mapped on the surface of NaOH-AD and NaOH-HD discs, respectively. The laser was focused using a 50×/0.5 NA objective and the Raman scattered light was collected with a Peltier-cooled charge-coupled device deep depletion near-infrared enhanced detector behind a 1200 g mm^{-1} grating. Raman maps were acquired at 5 μm step size, 1 s integration time, and 3 accumulations, preceded by 0.5 s bleaching time, generating 400 spectra on each surface. Additionally, a line measurement was made on the surface of an untreated cp-Ti disc at 5 μm step size generating 20 spectra. Data processing, including background subtraction and cosmic ray removal were performed in Renishaw WiRE 5.4 software. Elemental analysis was performed over ~100 μm^2 regions on NaOH-AD and NaOH-HD discs using EDX in a Quanta 200 environmental SEM (ESEM; FEI Company, The Netherlands) operated at a 15 kV accelerating voltage, 1 Torr water vapour pressure, and a 10 mm working distance. To assess the influence of heat treatment on the wettability, water contact angle to deionised water droplets (5 μl) was measured on NaOH-AD and NaOH-HD discs using an optical tensiometer (Attension Theta Flow, Biolin Scientific AB, Sweden).

The surface roughness of untreated machined cp-Ti, NaOH-AD, and NaOH-HD discs was measured using 3D SEM JEOL JSM-7800F Prime (JEOL, Japan) under a 5 kV accelerating voltage and a 10 mm working distance. In each of the three surfaces of interest, three distinct regions of 131.1 μm^2 were selected and stereoscopic pairs of SEM images acquired at a 10° angle difference. Surface roughness analysis was performed using MeX® software (Alicona Imaging GmbH, Austria) by generating a digital elevation model and applying a Gaussian filter to extract the topographical information. Surface roughness was expressed by S_a (averaged height of selected area) and S_{dr} (developed interfacial area ratio).

The stability and *in vitro* bioactivity of the alkali-modified surface was tested under physiologically relevant conditions.[42,43] NaOH-AD and NaOH-HD discs were submerged horizontally in 10 ml of Dulbecco's Modified Eagle's Medium (DMEM, Sigma Aldrich, USA) placed on an orbital shaker at 60 rpm in a temperature-controlled incubator at 37 °C for 28 days.

Afterwards, the discs were gently washed with deionised water, allowed to air dry, and Au sputter coated (10 nm). The discs were imaged with SEM (Ultra 55 FEG SEM, Leo Electron Microscopy Ltd, UK) using a 5 kV accelerating voltage and a 5 mm working distance. Calcium phosphate precipitation was confirmed using EDX in a Quanta 200 environmental SEM (FEI Company, The Netherlands) operated at a 15 kV accelerating voltage, 1 Torr water vapour pressure, and a 10 mm working distance. Point measurements (n = 7 per surface) were made on NaOH-AD and NaOH-HD discs.

Animal study

To investigate the influence of mechanical overload on osseointegration and mechanical stability of implants, we placed one NaOH-HD implant per tibia in female Sprague Dawley rats (n = 9, 320–350 g, Janvier, France). The animal experiments were approved by the Animal Research Ethics Committee of Gothenburg, Sweden (Dnr. 5.8.18-12983/2021) and adhered to ARRIVE guidelines. Animals had no restrictions on their movement and *ad libitum* access to standard rodent food.

All surgeries were performed under sterile conditions and animals were placed under general anaesthesia by 4% isoflurane inhalation. Animals were subcutaneously administered 0.03 mg kg^{-1} of buprenorphine analgesic (Temgesic®, Reckitt Benckiser Healthcare Limited, UK) just before surgery, and 8 h after the surgeries to alleviate the pain. In brief, the proximal tibial metaphysis was exposed, periosteum carefully removed, and bone defect prepared by successive drilling with low-speed round burs of 1.6 and 1.8 mm (∅) under profuse saline irrigation. The implants were unicortically inserted, the muscle and skin were repositioned and sutured. To achieve a stable osseointegration in rats, animals were allowed to heal for 28 days.[44] A second surgery was performed after 28 days of healing, where one implant per animal underwent a mechanical overload procedure. The implant was exposed, and soft tissue was carefully cleared to access the implant head for screwdriver placement. Using a T-handle attachment, a 90° clockwise snap-disruption of the bone–implant interface was performed, which was followed by an equal 90° counterclockwise rotation. All disruptions were performed by the same operator to minimise variability. To exclude the effect of soft tissue healing, the contralateral implant was exposed by performing a skin and muscle incision; however, the implant was kept undisrupted as a control. Finally, the muscle and skin were repositioned and sutured, and the animals were allowed to heal for an additional 28 days (Fig. 1).

Two calcium-binding fluorescent dyes, calcein and alizarin red (Sigma-Aldrich, USA), were subcutaneously injected into three animals. Calcein (at 10 mg kg^{-1}) was injected 3 days before the mechanical overload procedure, and alizarin red (at 25 mg kg^{-1}) was injected 21 days following the procedure.

At day 56, immediately upon euthanasia, the mechanical stability of disrupted and undisrupted implants was evaluated in six animals through removal torque (RTQ) measurements at a constant angular speed of 0.2° s^{-1}. In three animals, RTQ measurements were avoided to preserve the quality of the bone–implant interface. All implants with peri-implant bone were dissected *en bloc* and placed in 10% neutral buffered formalin prior to embedding in resin or paraffin (Table S1).

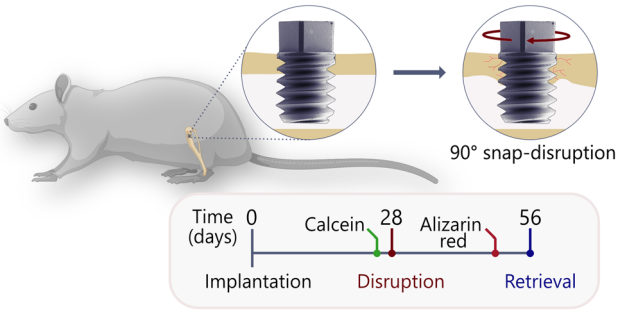

Fig. 1 Study strategy and timeline of the animal experiment.

X-ray micro-computed tomography, histology and histochemistry

After fixation, the retrieved implants with peri-implant bone (n = 6 per group) were dehydrated in a graded ethanol series (70–100% EtOH) and resin embedded (LR White Resin, London Resin Co. Ltd, UK). To assess the bone volume fraction within the implant threads (BV/TV), resin embedded samples were scanned using X-ray micro-computed tomography (micro-CT; Skyscan 1172, Bruker, Belgium) operated at 100 kV acceleration voltage and 100 μA current, for a 360° rotation, at an imaging resolution of 7.8 μm. Low-energy X-rays were blocked with Cu (40 μm) and Al (0.5 mm) filter. Reconstruction of the images was performed in NRecon software v.1.6.9.8 (Bruker, Belgium) and data analysis was performed using CTan software v.1.20.8.0+ (Bruker, Belgium).

Once scanned, the resin blocks were bisected, and one half was used for preparation of ground sections (using EXAKT cutting and grinding equipment; EXAKT Advanced Technologies GmbH, Germany). In samples collected from animals injected with fluorescent dyes (*i.e.*, calcein and alizarin red), first, ground sections of ~100 μm thickness were imaged using confocal laser scanning microscopy (CLSM; Nikon C2+ Nikon, Japan) using 525 and 785 nm laser emission wavelengths with a 20× objective to assess the integrity of the *in vivo* fluorescence labels. Then, all sections were polished to the final thickness of ~40 μm and stained with toluidine blue (1%) and basic fuchsin (1% methylene blue, 3% basic fuchsin). Undecalcified sections were imaged in Nikon Eclipse E600 optical microscope (Nikon Ltd, Japan) using 10×, 20×, and 40× objectives in a imaging software (NIS-Elements, Nikon Ltd, Japan) to determine the bone–implant contact (BIC, %) and bone area occupying the implant thread (B.Ar, %), and to evaluate the cellular response in bone of both disrupted and undisrupted samples.

The remaining *en bloc* samples of implants and peri-implant bone (n = 3 per group) were decalcified in ethylenediaminetetraacetic acid (EDTA) and dehydrated in a graded

ethanol series (70–100% EtOH). The decalcified bone was carefully separated from the implant and embedded in paraffin. Sections were cut to ~5 μm thickness, deparaffinised in xylene, and stained with hematoxylin and eosin (H&E). Further sections were made to evaluate osteoclastic activity and cell apoptosis by tartrate-resistant acid phosphatase assay (TRAP; Leukocyte Acid Phosphatase (TRAP) Kit, Sigma-Aldrich, USA), and terminal deoxynucleotidyl transferase dUTP nick end labelling (TUNEL; TUNEL Assay Kit – HRP-DAB, Abcam Limited, UK), respectively, according to manufacturer's protocols.

To examine the implant surface after 56 days *in vivo* and confirm if any tissue fragments remained attached, the implants retrieved after EDTA decalcification were stained with 1% osmium tetroxide and dehydrated in a graded ethanol series (70–100% EtOH), and Au sputter-coated (10 nm) for secondary electron SEM (Ultra 55 FEG SEM, Leo Electron Microscopy Ltd, UK) imaging, operated at a 5 kV accelerating voltage and a 5 mm working distance.

Quantitative backscattered electron imaging (qBEI)

Bone microstructure and mineralisation areas were examined on the remaining halves of resin-embedded sample blocks (n = 6 per group). The bisected blocks were polished using 400–4000 grit silicon carbide (SiC) paper, under water irrigation. The imaging was performed using backscattered electron scanning electron microscopy (BSE-SEM) in a Quanta 200 environmental SEM (FEI Company, The Netherlands) under a 20 kV accelerating voltage, 1 Torr water vapour pressure, and a working distance of 10 mm. The mineral content (Ca [wt%]) and bone mineral density distribution (BMDD) of bone within implant threads was evaluated using quantitative backscattered electron imaging (qBEI) following established protocols.[45] Using aluminium and carbon as calibration standards, brightness and contrast were adjusted to grey-level values of 225 for Al and 25 for C at 500× magnification. The calibrated, grey-level images were used to determine the weighted mean of Ca concentration (Ca_{MEAN}), the most frequent calcium concentration (Ca_{PEAK}), and the mineral heterogeneity as the full-width at half maximum under the BMDD curves (Ca_{WIDTH}).

Chemical composition of bone matrix

To assess the impact of mechanical overload on bone quality, Raman spectroscopy was performed on the same bisected, polished, resin-embedded blocks using a confocal Raman microscope (Renishaw inVia Qontor, Renishaw plc, UK) with a 785 nm laser and Live-Track focus-tracking technology to enhance signal stability.[46] In every sample, point measurements were made in the cortical bone within the implant thread keeping ~20 μm from the bone–implant interface. The laser was focused on the bone through a 100×/0.9 NA objective, and the Raman scattered light was collected using a Peltier-cooled charge-coupled device deep depletion near-infrared enhanced detector behind a 1200 g mm^{-1} grating. In the selected threads (n = 6 per group), 7 point-measurements were made at 5 s integration time and 3 accumulations with 0.5 s bleaching time.

Additionally, integral area maps were made in bone found in threads of representative undisrupted and disrupted implants. Following the polishing of bisected resin blocks, the surface of the samples labelled with fluorescence *in vivo* dyes was imaged by CLSM (Nikon C2$^+$, Nikon, Japan) at a laser emission wavelength of 525 nm and 785 nm using a 20× objective. By correlating CLSM and BSE-SEM images, ROIs for Raman imaging were selected to include both bone formed before disruption (*i.e.*, calcein labelled) and after disruption (*i.e.*, alizarin red labelled) within the implant thread. One map was acquired from an undisrupted implant (Map 1) and two maps (Maps 2 and 3) were acquired from a disrupted implant, comprising 3944, 2520, and 2262 spectra, respectively, at 1 μm step size, 1 s integration time and 3 accumulations with 1 s bleaching time. Background subtraction and cosmic ray removal were performed in Renishaw WiRE 5.4 software. Raman maps were evaluated based on the $\nu_1PO_4^{3-}$ peak intensity, normalised to the maximum value within each map. In all cases, spectra corresponding to the upper quartile of the $\nu_1PO_4^{3-}$ signal distribution were assigned to the high-mineralisation region. The low-mineralisation region was defined from the immediately preceeding range, excluding the lowest portion of the signal scale to avoid contributions from spectra generated in resin. Based on this segmentation, Map 1 included 2623 low- and 1269 high-mineralisation points, Map 2 included 494 and 1920 points, and Map 3 included 409 and 1742 points, respectively.

Three compositional parameters of bone were assessed: the mineral-to-matrix ratio, calculated as the integral area ratio of the $\nu_2PO_4^{3-}$ (~420–470 cm^{-1}) and amide III (~1240–1270 cm^{-1}) bands; the carbonate-to-phosphate ratio, taken as the intensity ratio of the $\nu_1CO_3^{2-}$ (~1070 cm^{-1}) and $\nu_1PO_4^{3-}$ (~960 cm^{-1}) peaks; and mineral crystallinity, taken as the inverse of full-width at half-maximum of the $\nu_1PO_4^{3-}$ peak and as intensity ratio of the $\nu_1PO_4^{3-}$ and $\nu_2PO_4^{3-}$ peaks.

Statistical analysis

Statistical analyses were performed using GraphPad Prism v10.0.0 (GraphPad Software, USA). The Welch's ANOVA test was used for surface roughness characterisation tests due to unequal variances among groups. The non-parametric, paired Wilcoxon test was used for comparisons between disrupted and undisrupted implants. In all tests, p-values <0.05 were considered statistically significant. Mean values ± standard deviations (SD) are presented.

Results

Material characterisation

Surface topography of alkali-modified discs and screw-shaped implants was examined by secondary electron SEM, which revealed an interconnected, submicron mesh-like surface on NaOH-AD and NaOH-HD (Fig. 2A). High hydrophilicity of the alkali-modified surface remained unchanged by subsequent heat drying treatment. The thickness of this fibrous layer was

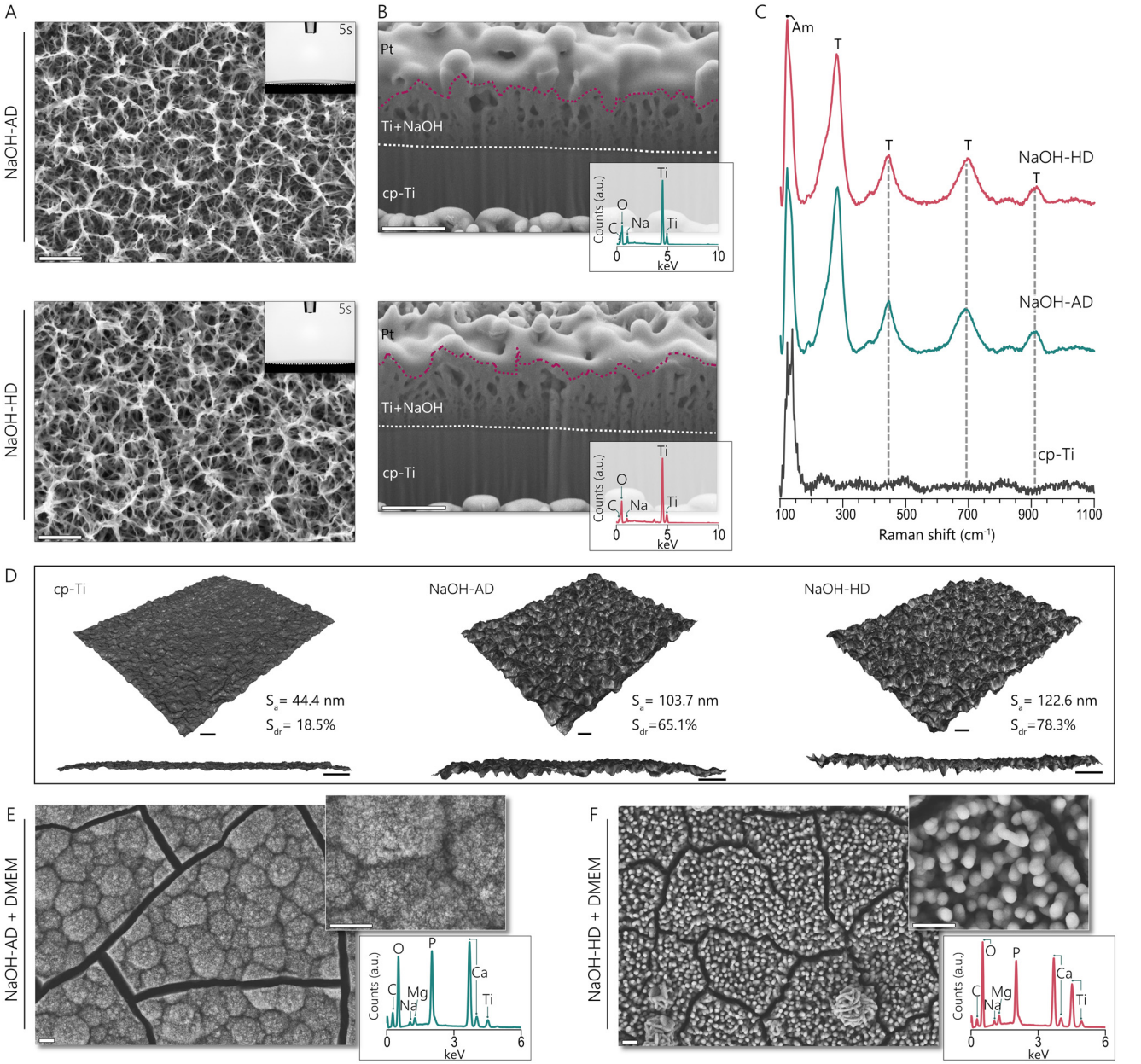

Fig. 2 Characterisation of alkali-modified Ti metal surfaces. (a) Surface topography of NaOH-AD and -HD discs. Insets—contact angle measurements at 5 s showing hydrophilic surface properties. (b) FIB SEM images showing the thickness of the NaOH-Ti gel layer. The white interrupted line demarcates the edge of the cp-Ti layer, magenta interrupted line demarcates the Pt layer from the NaOH-Ti gel layer. Insets—EDX spectra of both characterised surfaces show the presence of C, O, Na, and Ti. (c) Averaged Raman spectra of cp-Ti, NaOH-AD and -HD surfaces showing amorphous titanium oxide (Am) and titanate (T) characteristics peaks. (d) Surface roughness measurements of cp-Ti, NaOH-AD, and -HD surfaces. S_a = average height of the selected area, S_{dr} = the developed interfacial area ratio. Averages of three measurements. (e and f) SEM images of calcium phosphate formation on NaOH-AD (e) and NaOH-HD (f) surfaces following 28 days of immersion in DMEM. EDX spectra showing the presence of C, O, Na, Mg, Ca, P, and Ti. All scale bars = 1 μm.

~500 nm on both NaOH-AD and NaOH-HD discs, as measured on FIB-SEM images (Fig. 2B). EDX elemental mapping reveals the presence of O, Na, and Ti, with slightly higher Na/O ratio [at%] on NaOH-AD (~0.09) compared to NaOH-HD (~0.07) (Fig. 2B). Raman spectroscopy shows several sodium titanate peaks at ~270, 440, 690, and 909 cm^{-1} on both NaOH-AD and NaOH-HD (Fig. 2C). A peak at ~123 cm^{-1} is noted for all surfaces (*i.e.*, cp-Ti, NaOH-AD, and NaOH-HD), and is attributed to amorphous titanium oxide. Although the surface roughness does not differ substantially between NaOH-AD (S_a = 103.7 ± 9.3) and NaOH-HD (122.6 ± 36.5 nm), both alkali-modified surfaces exhibit significantly higher roughness ($p < 0.05$) compared to machined cp-Ti surface (S_a = 44.4 ± 3.6 nm) (Fig. 2D). The *in vitro* bioactivity of NaOH-AD and NaOH-HD was tested

by submersion in DMEM for 28 days. Calcium phosphate precipitation on both surfaces was confirmed by SEM and EDX, which showed the presence of Ca and P signals (Fig. 2E and F). In implants retrieved following decalcification with EDTA, the characteristic mesh-like surface topography of alkali-modified implant was observed on all samples, indicating that the surface treatment survives the implantation procedure, snap-disruption, and RTQ measurements (Fig. S1).

Animal experiment

Impact of mechanical overload on re-osseointegration of previously osseointegrated implants was evaluated after 28 days of re-healing (Fig. 3). At the 56-day endpoint, no statistically significant difference was found (p = 0.41) between the RTQ at the disrupted sites (9.4 ± 2.9 Ncm) and the undisrupted sites (8.7 ± 1.7 Ncm), indicating that the biomechanical stability had been recovered after the mechanical overload (Fig. 3B). The BV/TV of implant threads also did not differ significantly (p = 0.22) between the disrupted (41.2% ± 6.9%) and undisrupted sites (37.1% ± 5.7%) (Fig. 3C). Likewise, B.Ar measured on undecalcified histological sections did not show a considerable difference (p = 0.31) between the disrupted (65.3% ± 10.2%) and undisrupted (56.2% ± 12.6%) sites (Fig. 3D). The BIC was >75% at both disrupted (77.4% ± 8.3%) and undisrupted (83.5 ± 7.3%) sites (p = 0.31) (Fig. 3E).

Composition of bone within implant threads

BMDD was evaluated within implant threads of both disrupted and undisrupted implants (Fig. 4A). Using calibrated BSE-SEM images where each pixel represents a calcium concentration (Ca [wt%]), bone matrix composition was characterised by determining the Ca_{MEAN}, Ca_{WIDTH}, and Ca_{PEAK}. The BMDD measured between the two compared conditions showed no significant differences in any of the evaluated metrics (Fig. 4A). Extracellular bone matrix in close proximity to the implant threads was further evaluated using Raman spectroscopy (Fig. 4B), which revealed the typical spectral features representing the organic (proline, hydroxyproline, phenylalanine, and amide III) and inorganic ($\nu_1PO_4^{3-}$, $\nu_2PO_4^{3-}$, $\nu_1CO_3^{2-}$) components of bone. The compositional metrics associated with bone maturation, *i.e.*, the mineral-to-matrix ratio and the carbonate-to-phosphate ratio did not differ significantly between the disrupted and undisrupted sites. However, mineral crystallinity (1/FWHM $\nu_1PO_4^{3-}$) was lower in the undisrupted sites (p < 0.05) (Fig. 4B).

The impact of mechanical overload (*i.e.*, disruption) on surrounding bone was evaluated by *in vivo* labelling of ongoing bone formation using calcein and alizarin red, before and after disruption, respectively. Prior to histological staining, undecalcified ground sections (~100 μm thickness) were imaged using a CLSM. In bone proximal to implant surface of undisrupted implant sites, the integrity of the calcein band was preserved (Fig. 5A). In contrast, in bone associated with implants that underwent a mechanical overload, the observed calcein band was interrupted in several places and replaced with the alizarin band (Fig. 5A). Once imaged, undecalcified ground sections were further polished to thickness of ~40 μm

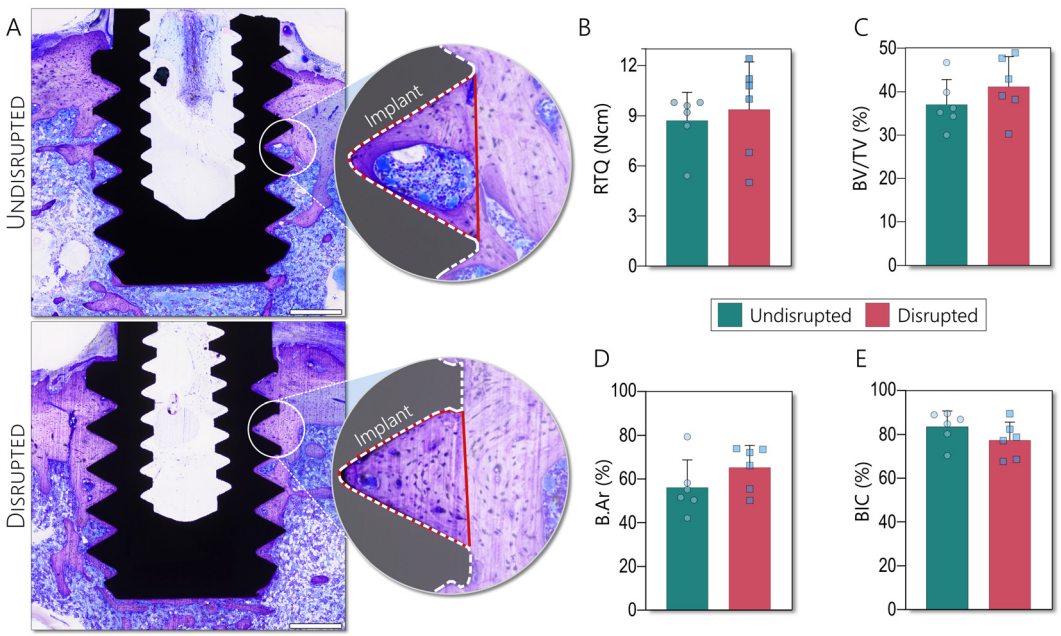

Fig. 3 Impact of mechanical overload on osseointegration. (a) Representative, undecalcified histological sections used for histomorphometry analyses. Insets show representative implant threads; the region of interest used for bone area (B.Ar) measurements is demarcated in red and the implant surface is marked with a dotted white line. Scale bars = 500 μm. (b) Removal torque (RTQ) measurements at the 56-day endpoint. (c) Three-dimensional evaluation of bone volume in total volume (BV/TV) of implant threads. (d) B.Ar measured within implant threads. (e) Bone–implant contact (BIC).

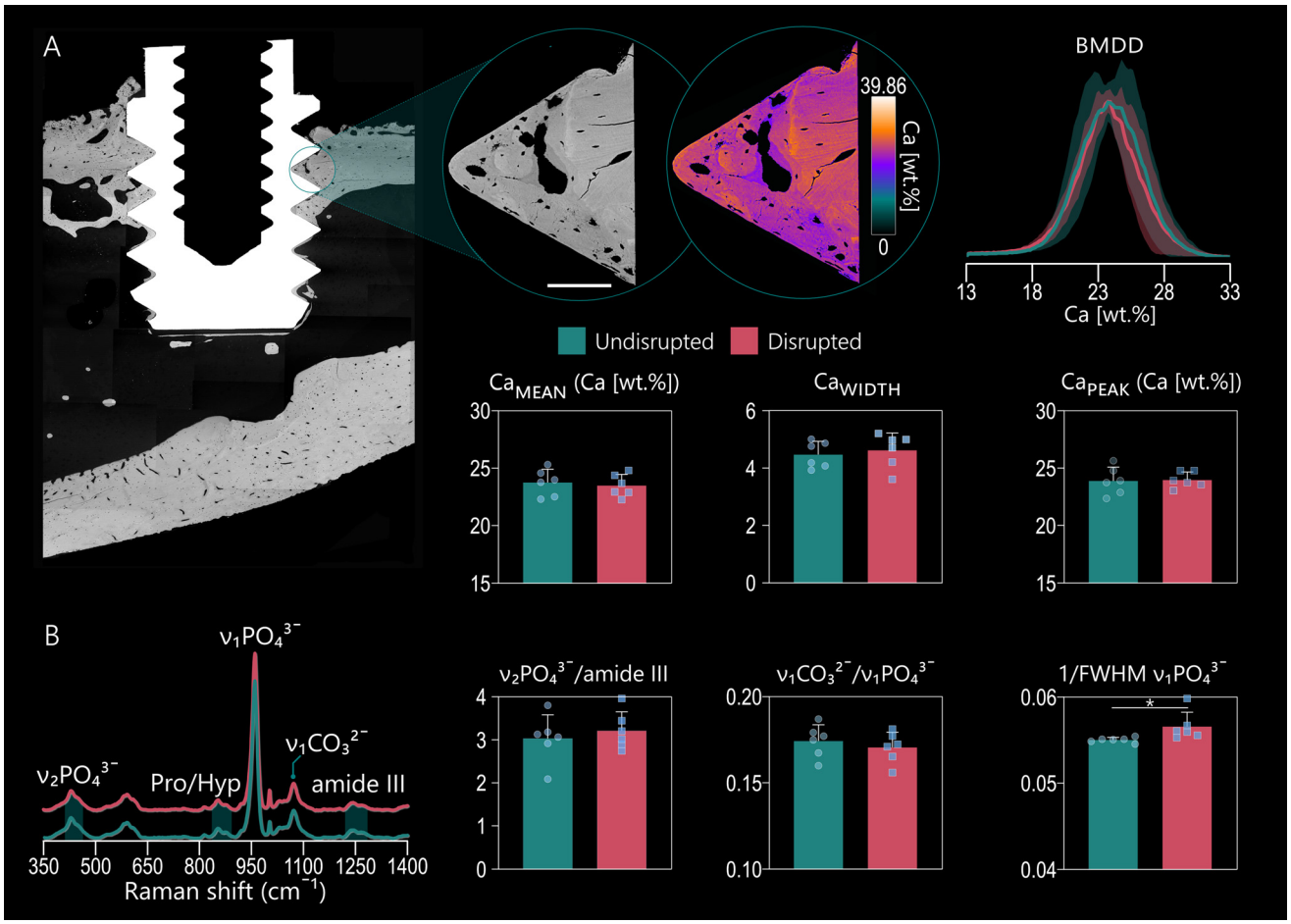

Fig. 4 Bone composition within the implant threads. (a) Bone mineral density distribution analysis (BMDD). Far left—representative BSE-SEM overview image. Inset—representative qBEI image with and without pseudo-colouring. Averaged BMDD curves generated from the histogram data of bone in threads of disrupted and undisrupted implants. BMDD metrics, from left to right: Ca_{MEAN}, Ca_{WIDTH}, and Ca_{PEAK}. Scale bar = 100 μm. (b) Chemical composition of bone ~20 μm from the implant surface. Averaged Raman spectra of bone within implant threads of disrupted and undisrupted implant sites showing apatite ($\nu_2PO_4^{3-}$ at ~420 to 470, $\nu_1PO_4^{3-}$ at ~960, and $\nu_1CO_3^{2-}$ ~1070 cm^{-1}) and collagen (proline, Pro, at ~855, hydroxyproline, Hyp, at ~876, and amide III at ~1240 to 1270 cm^{-1}). Raman metrics, from left to right: mineral-to-matrix ratio as the ratio of integral areas ($\nu_2PO_4^{3-}$/amide III), carbonate-to-phosphate ratio as the intensity ratio ($\nu_1CO_3^{2-}/\nu_1PO_4^{3-}$), and mineral crystallinity as the inverse of full-width at half-maximum of the $\nu_1PO_4^{3-}$ peak. * = $p < 0.05$.

and stained with toluidine blue-basic fuchsin stain. This allowed overlaying of fluorescence images and images of the same, subsequently stained, undecalcified sections with implant as a guide. Areas of bone labelled with alizarin red (*i.e.*, bone formed after the mechanical overload) corresponded to bone that was more intensely stained, whereas lighter staining of surrounding bone was observed in association with calcein labelled bone (*i.e.*, bone formed before the mechanical overload).

Similarly, using the implant as a guide, CLSM and BSE-SEM images were overlaid to select ROIs for Raman imaging that included both calcein and alizarin red labelled areas. In total, three maps were made, one in bone of undisrupted and two in bone of disrupted implant threads (Fig. 5B). Raman maps were normalised to the maximum value of the $\nu_1PO_4^{3-}$ peak and the areas of low and high $\nu_1PO_4^{3-}$ intensity were compared for different bone quality parameters (Fig. 5C). Bone labelled with alizarin red corresponded with low $\nu_1PO_4^{3-}$ intensity areas, while calcein labelled bone was not distinguishable from the surrounding bone in both undisrupted and disrupted implant sites. Higher mineral-to-matrix ratio and carbonate-to-phosphate ratio were calculated in high $\nu_1PO_4^{3-}$ intensity areas in all maps. Mineral crystallinity, taken as 1/FWHM of the $\nu_1PO_4^{3-}$ peak did not show differences between high- and low $\nu_1PO_4^{3-}$ intensity areas, the intensity ratio between $\nu_1PO_4^{3-}$ and $\nu_2PO_4^{3-}$ bands was consistently higher in the high $\nu_1PO_4^{3-}$ intensity areas.

Histological observations

The extent of *de novo* bone formation was evaluated using both undecalcified ground and decalcified paraffin sections (Fig. 6A). By 28 days after mechanical overload, stable osseointegration had been recovered and there were no obvious signs

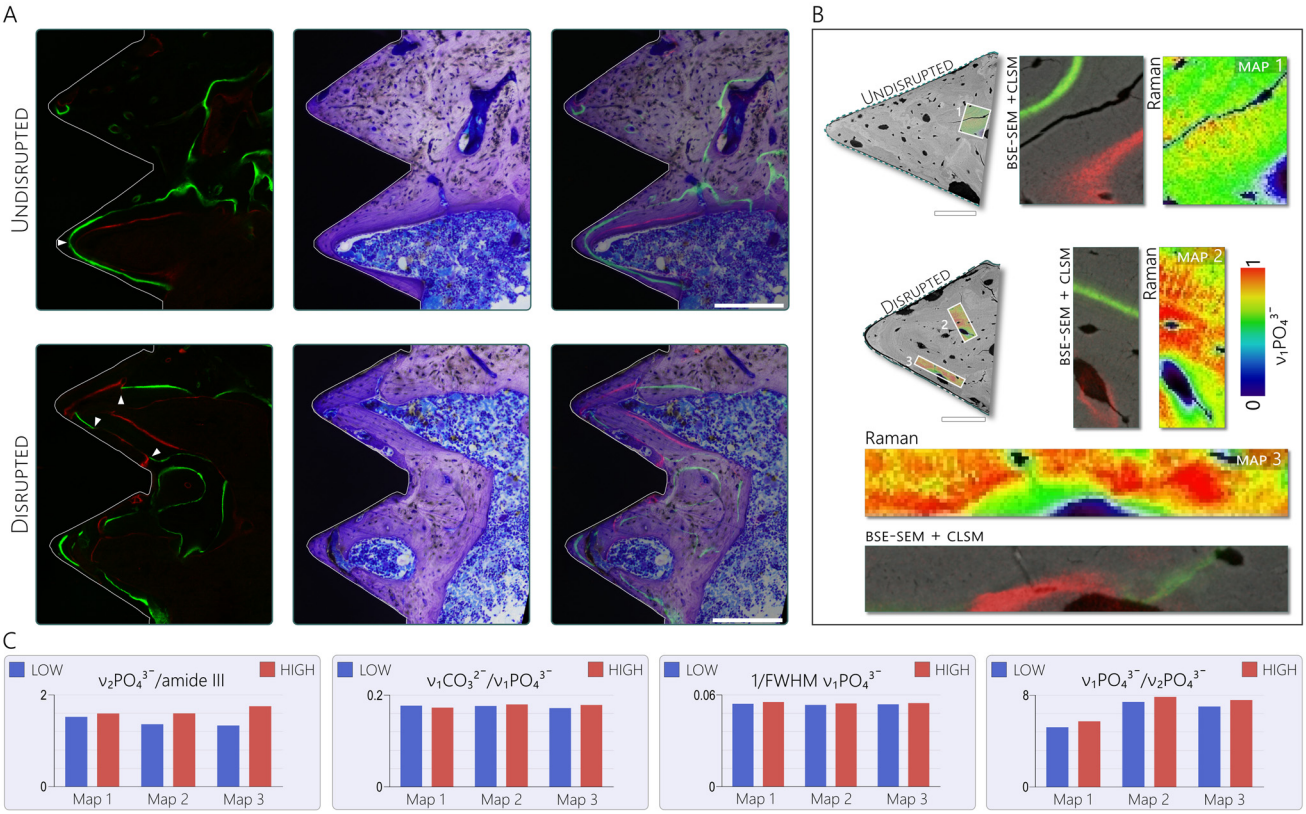

Fig. 5 Impact of mechanical overload on bone. (a) Left, fluorescence images of undecalcified sections prior to staining (~100 μm thickness). White arrowheads point towards undisrupted (upper panel) and disrupted (lower panel) calcein labels. Middle, same histological sections stained with basic fuchsin-toluidine blue (~40 μm thickness). Right, overlaid images. Scale bars = 200 μm. (b) Raman maps of the $\nu_1PO_4^{3-}$ peak intensity normalised to the maximum value detected in the map (1 μm per pixel). Maps were made in threads of undisrupted and disrupted implants. Areas of interest were selected by overlaying backscattered electron scanning electron microscopy (BSE-SEM) images with fluorescence images made using confocal laser scanning microscopy (CLSM). Scale bars = 100 μm. (c) Raman metrics calculated in areas of $\nu_1PO_4^{3-}$ low and high intensity. From left to right: mineral-to-matrix ratio as the ratio of integral areas ($\nu_2PO_4^{3-}$/amide III), carbonate-to-phosphate ratio as the intensity ratio ($\nu_1CO_3^{2-}/\nu_1PO_4^{3-}$), mineral crystallinity as the inverse of full-width at half-maximum of the $\nu_1PO_4^{3-}$ peak, and mineral crystallinity as the intensity ratio ($\nu_1PO_4^{3-}/\nu_2PO_4^{3-}$).

of ongoing extensive repair and/or remodelling processes. The long-term effects of implant disruption on cell viability were evaluated by labelling DNA fragmentation that occurs during cell apoptosis using TUNEL staining (Fig. 6B). Apoptotic cells were present in both the bone and the bone marrow. Disruption did not lead to an obvious increase in the incidence of apoptotic cells. TRAP staining confirmed the presence of active osteoclasts in bone of both disrupted and undisrupted samples (Fig. 6C). However, the prevalence of active osteoclastic cells was not higher in disrupted samples and their presence can be ascribed to homeostatic maintenance of bone tissue.

Discussion

In this work, we introduce a novel experimental model to study re-osseointegration of metal implants. In previously osseointegrated, submicron-roughened implants, an intentional disruption of bone–implant interface was introduced by traumatic loosening. A detailed description of the model, procedure, and results presented here shows that our model is well suited for studies of re-osseointegration. A combination of biomechanical, morphological, histological, and compositional analyses demonstrates that the complete re-osseointegration can be achieved, and that the peri-implant bone structure and composition do not bear the long-term consequences of disruption.

As opposed to line-of-sight methods for implant surface modification, such as selective laser-ablation,[33,47] alkali-modification alters the surface homogeneously and has been used in osseointegration studies.[36,38,40,41,48–50] Micro-roughened, alkali-modified implants are consistently more biomechanically stable than machined titanium implants.[36,48,50] Here, a typical submicron mesh-like topography was achieved with increased surface roughness and high hydrophilicity. Our goal was to create extensive bone–implant interlocking that would result in higher removal torque than that for machined implants. This level of interlocking was expected to induce microdamage in the peri-implant bone during snap-disrup-

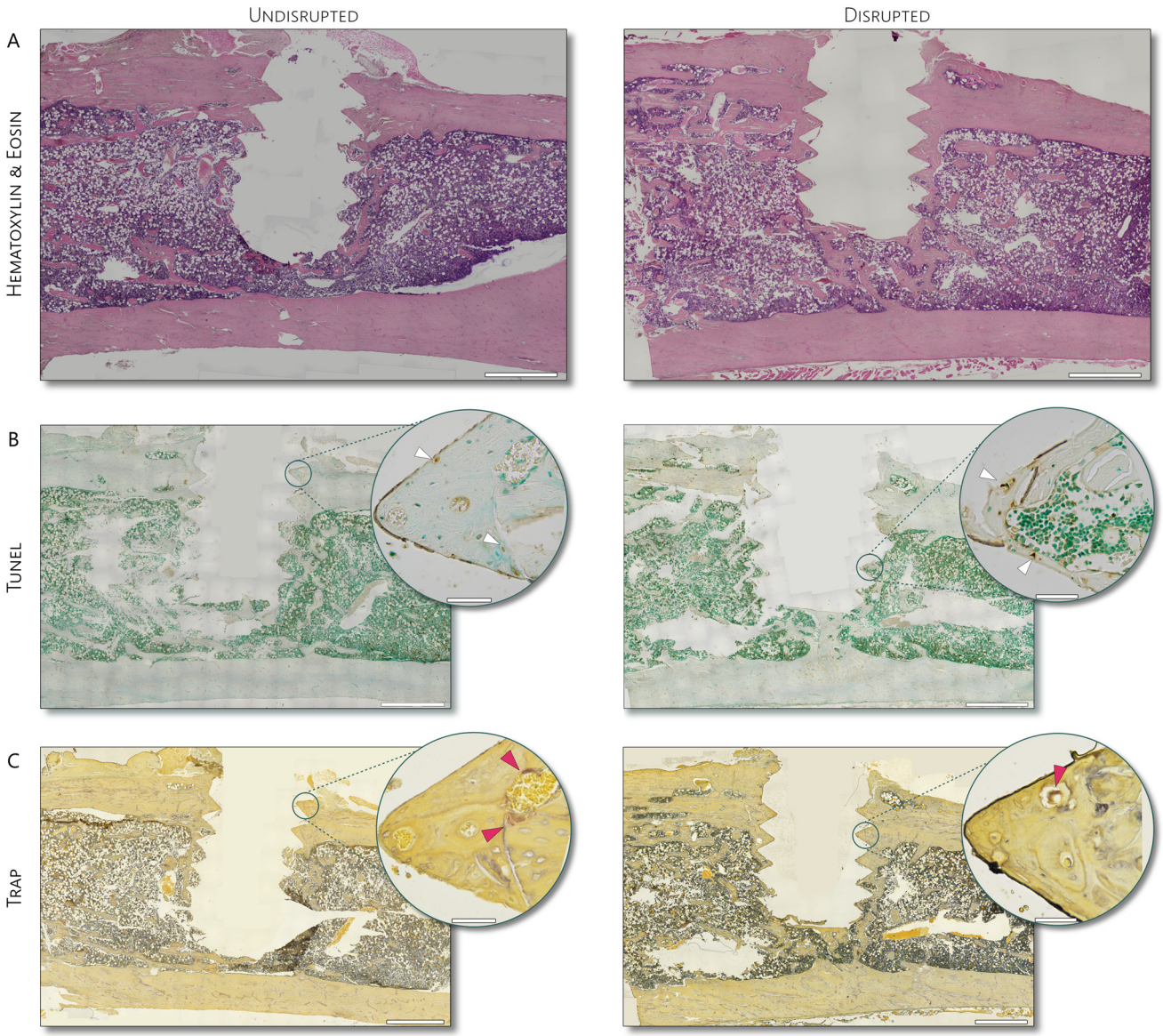

Fig. 6 Histological investigation of decalcified bone samples. (a) Hematoxylin & eosin-stained sections showing *de novo* bone formation within implant threads in both undisrupted and disrupted sites. (b) TUNEL (terminal deoxynucleotidyl transferase dUTP nick end) labelled sections; white arrowheads point towards apoptotic cells. (c) TRAP (tartrate-resistant acid phosphatase) labelled sections; red arrowheads point towards osteoclastic activity within the implant threads. Scale bars = 1 mm and 100 μm in insets.

tion, similar to effects previously observed after biomechanical testing of laser-ablated implants.[33]

We found that the bone–implant interlocking recovers after snap-disruption, and that the RTQ in disrupted implants even tends to be higher than in undisrupted implants. This pattern is consistent with previous observations of implants placed unicortically in rabbit tibiae, where disrupted implants had higher RTQ after 12 weeks of submerged healing.[27] In our model, the RTQ at 56 days *in vivo* is substantially higher for both disrupted and undisrupted implants compared to machined cp-Ti implants of similar diameter (⌀ 2 mm), also placed unicortically in rat tibiae, where RTQ values were 4.5 Ncm at 56 days and 6.5 Ncm after 112 days of undisrupted healing.[31]

Morphological parameters used to evaluate osseointegration such as BV/TV, or B.Ar and BIC[51] consistently showed similar values for both disrupted and undisrupted implants. In particular, the high BIC of both disrupted and undisrupted implants attests in favour of recovered osseointegration. Although biomechanical stability of implants measured by RTQ correlates positively with BIC,[52] it may also increase independently of the BIC, *e.g.*, due to progressive increase in mineral content and, consequently, increased extracellular matrix stiffness.[53] After 28 days of re-osseointegration, no sustained effects of snap-disruption on peri-implant bone mineralisation were reflected in BMDD parameters, *e.g.*, decreased mineral density due to remodelling. The same was true for

bone in the immediate proximity (*i.e.*, within ~20 μm) of the implant surface. The mineral-to-matrix ratio closely correlates with local calcium content assessed with qBEI[54] and reflects changes in the extracellular matrix composition associated with increase in mineral content with tissue age.[55,56] We found that the mineral content in bone around the disrupted implants tended to be higher than around the undisrupted implants. The incorporation of CO_3^{2-} into the apatite lattice with mineral maturity is used as another indicator of tissue age, expressed with carbonate-to-phosphate ratio.[57,58] B-type carbonate substitution can result in the decreased mineral crystallinity of synthetic carbonated apatites.[59] In the disrupted region, we found that the carbonate-to-phosphate ratio of bone at the implant interface was only slightly lower. However, mineral crystallinity calculated as 1/FWHM of the $\nu_1PO_4^{3-}$ peak was higher in the bone extracellular matrix of disrupted implant sites. A possible explanation for higher mineral crystallinity, is potential fragmentation of bone caused by snap-disruption event, during which small or larger fragments of bone become substrate for direct, new bone apposition and are not completely removed by bone remodelling processes. These fragments may continue to mineralise and could correspond with somewhat higher mineral-to-matrix ratio of the disrupted sites.

By labelling bone formation both before and after implant disruption, we confirmed that the snap-disruption caused sufficient damage to trigger targeted bone remodelling within the implant threads. The observed interruptions in the integrity of the calcein band indicate that micro-fractures appear at a small distance from the bone–implant junction. These areas undergo remodelling, where the affected bone is removed and new bone is deposited, as marked by alizarin red bands. Furthermore, alizarin red label coincides with intensely stained fuchsin-toluidine blue bone, indicative of younger extracellular matrix that is rich in acidic components such as acid phosphate (HPO_4^{2-}) and sulphated glycosaminoglycans. In both disrupted and undisrupted implant threads, the formation of new bone occurs quickly as alizarin bands (*i.e.*, bone formed 7 days prior study endpoint) are at a distance from the bone mineralisation front. Mineralisation occurs in two phases: rapid primary mineralisation and gradual secondary mineralisation.[60] High and low mineralisation areas were segmented using Raman maps (at 1 μm pixel size) of $\nu_1PO_4^{3-}$ peak intensity. Bone formed prior to disruption (*i.e.*, calcein labelled bone) was indistinguishable from the surrounding bone in the high mineralisation area. Bone formed juxtaposed between the alizarin red label and the mineralisation front corresponded to low mineralisation area. The lower mineral-to-matrix and carbonate-to-phosphate ratios in low mineralization regions are consistent with younger bone matrix.[60] However, mineral crystallinity (1/FWHM $\nu_1PO_4^{3-}$) did not differ substantially between low- and high mineralisation areas. It is known that 1/FWHM $\nu_1PO_4^{3-}$ is not always sensitive enough to detect subtle differences in mineral crystallinity due to the contribution from amorphous calcium phosphate at ~950 cm^{-1} (ref. 61 and 62) and broadening due to the disorder introduced by CO_3^{2-} incorporation with age.[57,58,63] As an alternative to 1/FWHM $\nu_1PO_4^{3-}$, the intensity of the $\nu_1PO_4^{3-}$ peak relative to the $\nu_2PO_4^{3-}$ (~420–450 cm^{-1}) band also provides additional insight into mineral crystallinity.[64,65] Here, we consistently calculated a higher $\nu_1PO_4^{3-}/\nu_2PO_4^{3-}$ ratio in high mineralisation areas, together with high carbonate-to-phosphate ratios, indicating that the mineral has attained a chronologically advanced stage. Note that a higher $\nu_1PO_4^{3-}/\nu_2PO_4^{3-}$ ratio, without a corresponding change in 1/FWHM $\nu_1PO_4^{3-}$ suggests that while the intrinsic crystallite size and structural order remain constant, a greater degree of crystallite co-alignment increases $\nu_1PO_4^{3-}$ intensity, particularly since the $\nu_1PO_4^{3-}$ band is sensitive to crystallographic orientation.[58]

Peri-implant bone completely recovers after the traumatic mechanical overload event, and by 28 days of healing, the bone around the disrupted implants is largely comparable to the bone around undisrupted implants. Histochemistry corroborates the morphological and compositional similarities between bone around disrupted and undisrupted implant. Neither TRAP staining, which evaluates osteoclastic activity in bone remodelling,[66] nor TUNEL staining, which indicates the presence of apoptotic cells,[67] revealed differences between disrupted and undisrupted peri-implant bone. This indicates that bone around disrupted implants arrives at a steady-state or homeostasis in the repair process, with no long-standing consequences on cellular activity or viability due to mechanical trauma induced by snap-disruption event. Provided that the imposed magnitude and duration of the mechanical stresses can be determined, the present model would allow for future interrogations into how mechanical cues influence cell behaviour at implant interfaces.

While findings from preclinical models cannot be directly extrapolated to human patients, similar biological responses are expected under comparable conditions,[68] as the core cellular mechanisms of bone healing and remodelling are conserved across vertebrates.[69] Rats exhibit a typical bone remodelling cycle of approximately 28 days,[70] compared to 120–200 days in humans,[71,72] making them particularly advantageous for studying implant healing within a condensed timeframe. The 28-day healing period selected in this study corresponds to a phase of stable osseointegration in rat models.[31,44] Although anatomical and physiological differences must be acknowledged, the rat provides a biologically relevant and accessible model for studying re-osseointegration. Moreover, the availability of established rat models with systemic conditions (*e.g.*, ovariectomised (OVX), Zucker Diabetic Fat (ZDF), and BB Wistar rats) enables investigations of re-osseointegration under compromised bone healing scenarios. For example, osteoporosis alters bone micro-architecture, turnover, and microdamage repair, reducing the implant anchorage.[53,73] Mechanical overload may further increase the risk of implant loosening in osteoporosis,[74] highlighting the clinical importance of re-osseointegration studies in such compromised conditions.

In this study, we present a new experimental model for investigating the impact of traumatic mechanical overload on

osseointegration, healing, and remodelling in peri-implant bone. While this study provides valuable insight into long-term outcomes of re-osseointegration following mechanical overload, early biological processes remain to be investigated. Future work should incorporate earlier post-disruption endpoints (*e.g.*, 3 and 7 days) and larger sample sizes, to examine the temporal dynamics of inflammation and early tissue repair. Emphasis should be placed on the molecular and cellular responses, including immune modulation and early osteogenic signalling at the bone–implant interface.

The correlative, multimodal analytical approach shows similar extracellular matrix composition, including an equilibrium in healing and/or remodelling when the implants are allowed to re-osseointegrate under aseptic conditions. The model presented here demonstrates that a single traumatic mechanical overload event does not trigger extensive bone resorption leading towards implant failure. However, caution is needed when extrapolating these findings to clinical scenarios where repeated or chronic overloads may occur. We unequivocally show that in absence of compromising systemic conditions, titanium implants can regain biomechanical stability after a mechanical overload event.

Author contributions

Martina Jolic: methodology, investigation, formal analysis, visualization, writing – original draft, writing – review and editing, funding acquisition. Paula Milena Giraldo-Osorno, Lena Emanuelsson, Birgitta Norlindh: methodology. Peter Thomsen: supervision, writing – review and editing, funding acquisition. Furqan A. Shah: conceptualization, investigation, supervision, writing – review and editing, funding acquisition. Anders Palmquist: conceptualization, methodology, investigation, supervision, writing – review and editing, funding acquisition. All authors have read and agreed to the published version of the manuscript.

Conflicts of interest

There are no conflicts to declare.

Data availability

The data supporting this article have been included as part of the supplementary information (SI). Supplementary information is available. See DOI: https://doi.org/10.1039/d5bm00502g.

Acknowledgements

This work was financially supported by the Swedish Research Council (2020-04715), the Svenska Sällskapet för Medicinsk Forskning (SSMF), the IngaBritt and Arne Lundberg Foundation (LU2024-0048), the Hjalmar Svensson Foundation, the Adlerbertska Foundation, the Kungliga Vetenskaps-och Vitterhets-Samhället i Göteborg, the Eivind och Elsa K:son Sylvans Stiftelse, the Swedish state under the agreement between the Swedish Government and the county councils, the ALF-agreement (ALFGBG-1005762), and the Area of Advance Materials of Chalmers and GU Biomaterials within the Strategic Research Area initiative launched by the Swedish government. This work was performed in part at the Chalmers Material Analysis Laboratory, CMAL. The funding sources had no role in the conceptualisation, design, data collection, analysis, decision to publish, or preparation of the manuscript.

References

1 R. Adell, U. Lekholm, B. Rockler and P. I. Brånemark, *Int. J. Oral Surg.*, 1981, **10**, 387–416.
2 F. A. Shah, P. Thomsen and A. Palmquist, *Acta Biomater.*, 2019, **84**, 1–15.
3 M. Esposito, J.-M. Hirsch, U. Lekholm and P. Thomsen, *Eur. J. Oral Sci.*, 1998, **106**, 527–551.
4 V. Drinias, G. Granström and A. Tjellström, *Clin. Implant Dent. Relat. Res.*, 2007, **9**, 94–99.
5 J. C. Park, W. S. Baek, S. H. Choi, K. S. Cho and U. W. Jung, *Clin. Oral Implants Res.*, 2017, **28**, 186–191.
6 M. Schimmel, M. Srinivasan, G. McKenna and F. Müller, *Clin. Oral Implants Res.*, 2018, **29**(Suppl 16), 311–330.
7 A. Mombelli and N. Cionca, *Clin. Oral Implants Res.*, 2006, **17**(Suppl 2), 97–103.
8 M. M. Bornstein, N. Cionca and A. Mombelli, *Int. J. Oral Maxillofac. Implants*, 2009, **24**(Suppl), 12–27.
9 T. Aghaloo, J. Pi-Anfruns, A. Moshaverinia, D. Sim, T. Grogan and D. Hadaya, *Int. J. Oral Maxillofac. Implants*, 2019, **34**, s35–s49.
10 M. Chang, V. Chronopoulos and N. Mattheos, *J. Investig. Clin. Dent.*, 2013, **4**, 142–150.
11 J. Duyck, H. J. Rønold, H. Van Oosterwyck, I. Naert, J. Vander Sloten and J. E. Ellingsen, *Clin. Oral Implants Res.*, 2001, **12**, 207–218.
12 K. Gotfredsen, T. Berglundh and J. Lindhe, *Clin. Oral Implants Res.*, 2001, **12**, 1–8.
13 K. Gotfredsen, T. Berglundh and J. Lindhe, *Clin. Oral Implants Res.*, 2001, **12**, 552–558.
14 E. De Smet, S. V. Jaecques, M. Wevers, J. A. Jansen, R. Jacobs, J. V. Sloten and I. E. Naert, *Eur. J. Oral Sci.*, 2006, **114**, 232–242.
15 P. Leucht, J. B. Kim, R. Wazen, J. A. Currey, A. Nanci, J. B. Brunski and J. A. Helms, *Bone*, 2007, **40**, 919–930.
16 M. Esposito, J. M. Hirsch, U. Lekholm and P. Thomsen, *Eur. J. Oral Sci.*, 1998, **106**, 527–551.
17 Y. T. Hsu, J. H. Fu, K. Al-Hezaimi and H. L. Wang, *Int. J. Oral Maxillofac. Implants*, 2012, **27**, 894–904.
18 J. Duyck and K. Vandamme, *J. Oral Rehabil.*, 2014, **41**, 783–794.

19 W. F. Zimmerman, M. A. Miller, R. J. Cleary, T. H. Izant and K. A. Mann, *J. Biomech.*, 2016, **49**, 2068–2075.
20 Socialstyrelsen, Statistikdatabasen, https://www.socialstyrelsen.se/statistik-och-data/statistik/statistikdatabasen/.
21 T. S. A. Register, Annual Report 2023, https://registercentrum.blob.core.windows.net/sar/r/SAR_Annual-report-2023_ENDS5gryeOB.pdf, (accessed 2025-09-24, 2025).
22 S. Svenskt, Kvalitetsregister för Karies och Parodontit, ÅRSRAPPORT 2023, https://www.skapareg.se/wp-content/uploads/2024/08/SKaPa-%C3%85rsrapport-2023.pdf, (accessed 2025-09-24, 2025).
23 M. Sundfeldt, L. V. Carlsson, C. B. Johansson, P. Thomsen and C. Gretzer, *Acta Orthop.*, 2006, **77**, 177–197.
24 R. Chowdhary, N. Chowdhary and S. K. Mishra, *Niger. J. Clin. Pract.*, 2011, **14**, 102–105.
25 N. Mattheos, M. Schittek Janda, A. Zampelis and V. Chronopoulos, *Clin. Oral Implants Res.*, 2013, **24**, 347–354.
26 C. Gstoettner, S. Salminger, A. Sturma, V. Moser, T. Hausner, R. Brånemark and O. C. Aszmann, *Prosthet. Orthot. Int.*, 2021, **45**, 76–80.
27 C.-J. Ivanoff, L. Sennerby and U. Lekholm, *Int. J. Oral Maxillofac. Surg.*, 1997, **26**, 310–315.
28 J.-H. Jang, J. H. Cho and C. H. Lee, *J. Korean Acad. Prosthodont.*, 2010, **48**, 209–214.
29 S.-H. Ye, J.-H. Cho and C.-H. Lee, *J. Dent. Rehabil. Appl. Sci.*, 2015, **31**, 203–211.
30 S. Kim, J.-S. Lee, J.-W. Hwang, M.-S. Kim, S.-H. Choi and U.-W. Jung, *Clin. Oral Implants Res.*, 2014, **25**, 729–734.
31 R. Brånemark, L.-O. Öhrnell, P. Nilsson and P. Thomsen, *Biomaterials*, 1997, **18**, 969–978.
32 X. Liu, P. K. Chu and C. Ding, *Mater. Sci. Eng., R*, 2004, **47**, 49–121.
33 R. Brånemark, L. Emanuelsson, A. Palmquist and P. Thomsen, *Nanomedicine*, 2011, **7**, 220–227.
34 K. Grandfield, S. Gustafsson and A. Palmquist, *Nanoscale*, 2013, **5**, 4302–4308.
35 H. M. Kim, F. Miyaji, T. Kokubo and T. Nakamura, *J. Biomed. Mater. Res.*, 1996, **32**, 409–417.
36 S. Nishiguchi, S. Fujibayashi, H.-M. Kim, T. Kokubo and T. Nakamura, *J. Biomed. Mater. Res., Part A*, 2003, **67**, 26–35.
37 T. Kokubo, H. M. Kim, M. Kawashita and T. Nakamura, *J. Mater. Sci.: Mater. Med.*, 2004, **15**, 99–107.
38 J.-W. Park, I.-S. Jang and J.-Y. Suh, *J. Biomed. Mater. Res., Part B*, 2008, **84**, 400–407.
39 L. Lin, H. Wang, M. Ni, Y. Rui, T.-Y. Cheng, C.-K. Cheng, X. Pan, G. Li and C. Lin, *J. Orthop. Translat.*, 2014, **2**, 35–42.
40 W. A. Camargo, S. Takemoto, J. W. Hoekstra, S. C. G. Leeuwenburgh, J. A. Jansen, J. J. J. P. van den Beucken and H. S. Alghamdi, *Acta Biomater.*, 2017, **57**, 511–523.
41 S. Fujibayashi, T. Nakamura, S. Nishiguchi, J. Tamura, M. Uchida, H.-M. Kim and T. Kokubo, *J. Biomed. Mater. Res.*, 2001, **56**, 562–570.
42 F. A. Shah, D. S. Brauer, R. M. Wilson, R. G. Hill and K. A. Hing, *J. Biomed. Mater. Res., Part A*, 2014, **102**, 647–654.
43 T. Kokubo and H. Takadama, *Biomaterials*, 2006, **27**, 2907–2915.
44 D. Karazisis, L. Rasmusson, S. Petronis, A. Palmquist, F. A. Shah, H. Agheli, L. Emanuelsson, A. Johansson, O. Omar and P. Thomsen, *Acta Biomater.*, 2021, **136**, 279–290.
45 P. Roschger, E. P. Paschalis, P. Fratzl and K. Klaushofer, *Bone*, 2008, **42**, 456–466.
46 F. A. Shah, K. Ruscsák and A. Palmquist, *Cells Tissues Organs*, 2021, **209**, 266–275.
47 J. Frostevarg, R. Olsson, J. Powell, A. Palmquist and R. Brånemark, *Appl. Surf. Sci.*, 2019, **485**, 158–169.
48 S. Nishiguchi, T. Nakamura, M. Kobayashi, H.-M. Kim, F. Miyaji and T. Kokubo, *Biomaterials*, 1999, **20**, 491–500.
49 S. Nishiguchi, H. Kato, M. Neo, M. Oka, H.-M. Kim, T. Kokubo and T. Nakamura, *J. Biomed. Mater. Res.*, 2001, **54**, 198–208.
50 C.-S. Chang, T.-M. Lee, C.-H. Chang and J.-K. Liu, *Clin. Oral Implants Res.*, 2009, **20**, 1178–1184.
51 L. Sennerby, P. Thomsen and L. Ericson, *J. Mater. Sci.: Mater. Med.*, 1993, **4**, 240–250.
52 F. A. Shah, M. L. Johansson, O. Omar, H. Simonsson, A. Palmquist and P. Thomsen, *PLoS One*, 2016, **11**, e0157504.
53 M. Jolic, S. Sharma, A. Palmquist and F. A. Shah, *Heliyon*, 2022, **8**, e10844.
54 A. Roschger, S. Gamsjaeger, B. Hofstetter, A. Masic, S. Blouin, P. Messmer, A. Berzlanovich, E. P. Paschalis, P. Roschger, K. Klaushofer and P. Fratzl, *J. Biomed. Opt.*, 2014, **19**, 065002.
55 E. Donnelly, D. X. Chen, A. L. Boskey, S. P. Baker and M. C. van der Meulen, *Calcif. Tissue Int.*, 2010, **87**, 450–460.
56 F. A. Shah, K. Ruscsak and A. Palmquist, *Bone Rep.*, 2020, **13**, 100283.
57 S. Uppuganti, M. Granke, A. J. Makowski, M. D. Does and J. S. Nyman, *Bone*, 2016, **83**, 220–232.
58 S. Gamsjaeger, A. Masic, P. Roschger, M. Kazanci, J. W. Dunlop, K. Klaushofer, E. P. Paschalis and P. Fratzl, *Bone*, 2010, **47**, 392–399.
59 J. D. McElderry, P. Zhu, K. H. Mroue, J. Xu, B. Pavan, M. Fang, G. Zhao, E. McNerny, D. H. Kohn, R. T. Franceschi, M. M. Holl, M. M. Tecklenburg, A. Ramamoorthy and M. D. Morris, *J. Solid State Chem.*, 2013, **206**, 192–198.
60 E. Donnelly, A. L. Boskey, S. P. Baker and M. C. H. van der Meulen, *J. Biomed. Mater. Res., Part A*, 2010, **92**, 1048–1056.
61 N. J. Crane, V. Popescu, M. D. Morris, P. Steenhuis and M. A. Ignelzi, *Bone*, 2006, **39**, 434–442.
62 J. A. Stammeier, B. Purgstaller, D. Hippler, V. Mavromatis and M. Dietzel, *MethodsX*, 2018, **5**, 1241–1250.
63 B. Wopenka and J. D. Pasteris, *Mater. Sci. Eng., C*, 2005, **25**, 131–143.
64 F. A. Shah, *Sci. Rep.*, 2020, **10**, 16662.

65 F. A. Shah, *Sci. Rep.*, 2023, **13**, 12301.
66 M. Haga, N. Fujii, K. Nozawa-Inoue, S. Nomura, K. Oda, K. Uoshima and T. Maeda, *Anat. Rec.*, 2009, **292**, 38–47.
67 A. L. Bronckers, W. Goei, G. Luo, G. Karsenty, R. N. D'Souza, D. M. Lyaruu and E. H. Burger, *J. Bone Miner. Res.*, 1996, **11**, 1281–1291.
68 A. Stavropoulos, A. Sculean, D. D. Bosshardt, D. Buser and B. Klinge, *Periodontol 2000*, 2015, **68**, 55–65.
69 A. H. Doherty, C. K. Ghalambor and S. W. Donahue, *Physiology*, 2015, **30**, 17–29.
70 R. G. Erben, *Anat. Rec.*, 1996, **246**, 39–46.
71 M. O. Agerbaek, E. F. Eriksen, J. Kragstrup, L. Mosekilde and F. Melsen, *Bone Miner.*, 1991, **12**, 101–112.
72 J. Kenkre and J. Bassett, *Ann. Clin. Biochem.*, 2018, **55**, 308–327.
73 R. Eastell, T. W. O'Neill, L. C. Hofbauer, B. Langdahl, I. R. Reid, D. T. Gold and S. R. Cummings, *Nat. Rev. Dis. Primers*, 2016, **2**, 16069.
74 M. Daher, E. Mekhael and M. M. El-Othmani, *Hip Pelvis*, 2024, **36**, 260–272.